


Article

CO₂ Interaction Mechanism of SnO₂-Based Sensors with Respect to the Pt Interdigital Electrodes Gap

Adelina Stanoiu ¹, Alexandra Corina Iacoban ¹, Catalina Gabriela Mihalcea ^{1,2}, Ion Viorel Dinu ¹, Ovidiu Gabriel Florea ¹, Ioana Dorina Vlaicu ¹ and Cristian Eugen Simion ^{1,*} 

¹ National Institute of Materials Physics, Atomistilor 405A, 077125 Magurele, Romania; adelina.stanoiu@infim.ro (A.S.); alexandra.iacoban@infim.ro (A.C.I.); catalina.mihalcea@infim.ro (C.G.M.); vdinu@infim.ro (I.V.D.); ovidiu.florea@infim.ro (O.G.F.); ioana.vlaicu@infim.ro (I.D.V.)

² Faculty of Physics, University of Bucharest, Atomistilor 405, 077125 Magurele, Romania

* Correspondence: simion@infim.ro; Tel.: +40-21-2418134

Abstract: The tuning sensitivity towards CO₂ detection under in-field-like conditions was investigated using SnO₂-sensitive material deposited onto Al₂O₃ substrates provided with platinum electrodes with interdigital gaps of 100 μm and 30 μm. X-ray diffraction, low-magnification and high-resolution transmission electron microscopy, and electrical and contact potential difference investigations were employed to understand the sensing mechanism involved in CO₂ detection. The morpho-structural analysis revealed that the SnO₂ nanoparticles exhibit well-defined facets along the (110) and (101) crystallographic planes. Complex phenomenological investigations showed that moisture significantly affects the gas sensing performance. The experimental results corroborated the literature evidence, highlighting the importance of Pt within the interdigital electrodes subsequently reflected in the increase in the CO₂ sensing performance with the decrease in the interdigital gap. The catalytic efficiency is explained by the distribution of platinum at the gas-Pt-SnO₂ three-phase boundary, which is critical for enhancing the sensor performance.

Keywords: SnO₂ nanoparticles; CO₂ sensitivity; platinum electrodes; variable interdigital gap; catalytic activity of platinum electrodes



Citation: Stanoiu, A.; Iacoban, A.C.; Mihalcea, C.G.; Dinu, I.V.; Florea, O.G.; Vlaicu, I.D.; Simion, C.E. CO₂ Interaction Mechanism of SnO₂-Based Sensors with Respect to the Pt Interdigital Electrodes Gap. *Chemosensors* **2024**, *12*, 238. <https://doi.org/10.3390/chemosensors12110238>

Received: 24 September 2024
Revised: 8 November 2024
Accepted: 14 November 2024
Published: 16 November 2024



Copyright: © 2024 by the authors. Licensee MDPI, Basel, Switzerland. This article is an open access article distributed under the terms and conditions of the Creative Commons Attribution (CC BY) license (<https://creativecommons.org/licenses/by/4.0/>).

1. Introduction

The origin of metal oxide semiconductor (MOS)-based gas sensors may be traced back to the early 1970s, when Taguchi introduced the first gas sensing device utilising tin dioxide (SnO₂) [1]. In addition to its use as a transparent coating element for electrode material in solar cells or displays, SnO₂ is primarily involved in gas sensing and catalysis. The SnO₂-based sensors have been utilised in various industrial sectors, including automotive, chemical, environmental detection and control, food, medicine, military, and safety. The initial requirement involves monitoring the emissions from the vehicle, which mostly consist of carbon in the form of small particles, unburned hydrocarbons, carbon dioxide, carbon monoxide, nitrogen oxides, sulphur oxides, water vapour, and various other low-level chemicals. The need to monitor the levels of different gases has led to extensive research and development efforts to create sensors based on SnO₂ that are widely applicable in various fields [2]. Moreover, there are plenty of studies related to doped or un-doped SnO₂ specific to the aforementioned target sectors. When it comes to the detection of carbon dioxide (CO₂), MOS-based gas sensors are almost insensitive under normal working in-field conditions (e.g., the presence of oxygen and relative humidity—RH).

Carbon dioxide is an inert gas that absorbs short-wavelength light, contributing significantly to the greenhouse effect. It is commonly found in the atmosphere at concentrations between 300 and 400 parts per million (ppm). As the concentration of CO₂ in the environment rises, the human body will progressively encounter discomfort, difficulty breathing,

impaired sensory function, dizziness, shock, and perhaps death [3]. Monitoring the concentration of CO₂ in respiration can provide valuable insights into respiratory status and circulation disorders [4]. It can also help in the timely detection of respiratory dysfunction and other abnormal situations during general anaesthesia, making it highly valuable in both the operating room and the intensive care department [5]. From an industrial perspective, the extensive utilisation of fossil fuels leads to an increase in the concentration of CO₂ in the atmosphere. Hence, the monitoring of CO₂ is interconnected with the well-being, health, and safety of individuals, as well as the government's oversight of carbon emissions and precise decision-making regarding energy structure regulation [6].

Currently, CO₂ detection is performed with optical sensors [7], resistive sensors [8], potentiometric sensors [9], amperometric sensors [10], capacitive sensors [11], surface acoustic wave sensors [12], and quartz crystal microbalance sensors [13], among others. Chemical gas sensors, which rely on the changes in the electrical resistance (conductance) of MOS under variable surrounding conditions, are the simplest, cheapest, and most user-friendly alternative [14]. In this respect, binary and ternary MOSs with high porosity, a large specific surface area, and defect structures have attracted the attention of researchers. For instance, ternary metal oxides exhibit Schottky, Frenkel, and interstitial atom defects, due to variations in crystal structure, cation species, and valence states. In addition, the presence of doped cations occupying the A/B sites will result in the formation of certain non-intrinsic defects, which in turn contribute to the absorption of the target gas. The primary ternary metal oxide materials utilised for CO₂ sensing are the perovskite structure (ABO₃) and spinel structure (AB₂O₄) oxides. These include barium titanate (BaTiO₃), lanthanum ferrite (LaFeO₃), nickel ferrite (NiFe₂O₄), and magnesium ferrite (MgFe₂O₄). Typically, they are manufactured to create integrated structures or heterostructures by combining them with metal oxides to improve their gas-sensing abilities [15,16]. In the work of Chavali et al., metal oxide nanoparticles are described by their gas-sensing performance concerning hierarchical structure, shape, and size. Not only the gas-sensing applications are discussed, but also their complex applications in nanotechnologies [17]. Unfortunately, the atmospheric relative humidity (RH) significantly affects the absorption and release of carbon dioxide. The impact of RH on the sensing mechanism was investigated using density functional theory (DFT). Under conditions of low humidity (RH < 35%), the interaction between carbon dioxide (CO₂) and tin dioxide (SnO₂) with pre-adsorbed oxygen ions (O²⁻ and O⁻) from the (110) crystal surface was minimal. At a higher RH, CO₂ molecules were adsorbed onto the (110) crystal surface of SnO₂. During this process, CO₂ reacts with OH⁻ ions (from the dissociative adsorption of water) and leads to the formation of carbonate. Additionally, an exchange of electrons between CO₂ and SnO₂ occurs. The results suggest that the pre-adsorbed OH⁻ on the (110) crystal facet enhances the CO₂ sensing properties [18]. This indicates that certain crystal surfaces have a strong ability to adsorb or react with various atomic, ionic, and molecular groups. Xiong et al. investigated the sensing properties of SnO₂ films doped with La, Gd, and Lu, as well as pure SnO₂ films, for the detection of CO₂ in an environment devoid of oxygen [19]. La significantly enhanced the performance of CO₂ sensing, with the highest performance observed when the La doping content reached 4%. The rate at which carbonates develop and the amount of oxygen vacancies have a significant impact on the features of gas sensing. Consequently, the researchers analysed the XPS spectra of the O 1 s and C 1 s samples. They then determined the ratio of peak areas for residual carbon (organic carbon pollution) and carbonates, as well as the ratio of peak areas for oxygen (O⁻ and O²⁻). The optimal doping ratio was determined to be 8 at. % when the concentrations of O₂ in the carrier gas reached 21% (in-field oxygen level), and it should increase to 16 at.% in the presence of free oxygen.

In the present study, we aimed to address a realistic scenario of the gas-surface interaction mechanisms involved in CO₂ detection under in-field-like conditions characterised by the presence of oxygen and variable relative humidity. Therefore, we performed DC electrical investigations and simultaneous electrical resistance measurements assisted by the

contact potential differences on planar sensors, which were obtained by screen-printed SnO₂ thick layers on substrates with different interdigital gaps of 100 and 30 μm, respectively.

2. Materials and Methods

2.1. Powders Synthesis

As previously reported [20], a sodium hydroxide solution was added dropwise over a solution of tin (IV) chloride containing CTAB (hexadecyltrimethylammonium bromide). The mixture was stirred for half an hour at room temperature, was afterward sealed in a Hydrothermal Synthesis Autoclave Reactor with a PTFE Lined Vessel of 100 mL, and was left to react at 160 °C for 18 h. SnO₂ powder was isolated by centrifugation, washed repeatedly, and air-dried at 120 °C. To complete the synthesis process, the dried powder was thermally treated at 550 °C. The chemicals were used as purchased, without any further purification: tin (IV) chloride (SnCl₄, 99.999%, Acros Organics, Geel, Belgium), sodium hydroxide (NaOH, >98%, Honeywell Fluka, Seelze, Germany), and hexadecyltrimethylammonium bromide (CTAB, 99%, Acros Organics, Geel, Belgium). A final thermal treatment at 550 °C has completed the preparation processes.

2.2. Structural and Morphological Investigations

Structural investigations were performed using powder X-ray diffraction with a D8 ADVANCE diffractometer (BRUKER-57AXS GmbH, Karlsruhe, Germany) with Ni-filtered Cu radiation ($\lambda = 1.54184 \text{ \AA}$) at room temperature in Bragg–Brentano geometry in the range of 2θ from 20° to 95°. The XRD data were analysed using the Rietveld refinement with MAUD version 2.99 software to determine the lattice parameters and average crystallite size.

The morphology of the SnO₂ sample was investigated using a JEOL JEM-ARM200F transmission electron microscope (JEOL LTT., Japan, Tokyo), operated at 200 kV. To prepare the TEM sample, a small quantity of the powder was mixed with ethanol, then it was ultra-sonicated for 10 min, and a small droplet from this mix was drop-cast on a TEM copper grid provided with a carbon membrane.

2.3. Layer Deposition and Sensing Investigations

The layer deposition process is the subject of a national patent application, OSIM/Nr. A 00110/18 March 2024. In brief, the as-prepared sensitive powders were combined with 1,2 Propanediol and grounded to produce a paste with a medium viscosity. Subsequently, the paste was applied onto commercial alumina substrates using the screen-printing technique to form thick layers. The sensors obtained were gradually dehydrated and thermally treated at 500 °C in air. This procedure enables the thorough elimination of the organic solvent, guaranteeing the porosity of the layer and enhancing its adhesion to the substrate. The alumina substrates are made using planar technology and are provided with platinum electrodes and a heater on the backside. The interdigital electrodes on the substrate have gaps measuring 100 μm and 30 μm, respectively. The obtained samples were labelled “SnO₂ 100 μm” and “SnO₂ 30 μm”. The electrical power through the heater is adjusted to control the temperature of the sensor layer, which in turn modulates the chemical interaction between the MOS layer and the test gases. The substrates were passivated with glass on both sides to avoid parasitic catalytic effects, thus highlighting the catalytic processes that are taking place solely on the sensitive layer or at the three-phase boundary (e.g., gas–electrodes–SnO₂).

A Gas Mixing System (GMS) was used to simulate the in-field atmosphere (Figure 1). The GMS is managed by specialised software and comprises eleven gas channels fitted with mass flow controllers, solenoid valves, and high-purity gas bottles. The system functions in a dynamic state, maintaining a total flow rate of 200 mL/min. A relative humidity (RH) is accomplished using a distinct pathway involving a gas-washing bottle containing moisture. The real-time acquisition of the electrical resistance changes in sensors positioned inside the sensor chamber was performed using a dedicated electrometer Keithley 6517A (Tektronix, OHIO, Solon, OH, USA) operated under constant 3V bias, while the contact

potential differences (CPD) were recorded using a McAllister 6500 Kelvin Probe (McAllister Technical Services, CALIFORNIA, Berkeley, CA, USA).

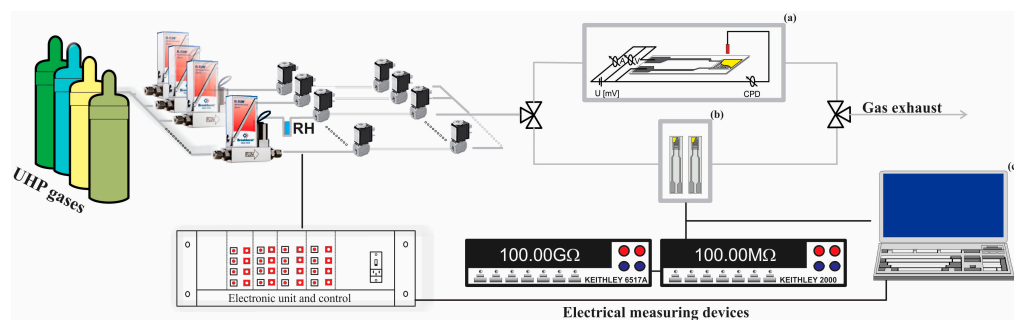


Figure 1. Gas Mixing System provided with a Kelvin probe involved in DC and contact potential difference measurements (a), a sensor chamber (b), and a PC dedicated to evaluation and control (c).

3. Results and Discussions

3.1. XRD Characterisation

The powder X-ray diffraction (XRD) of the SnO_2 sample prepared by the hydrothermal method at a temperature of $160\text{ }^\circ\text{C}$ presents the characteristic diffraction lines of the SnO_2 (Figure 2). It exhibits a tetragonal structure with a symmetry space group of $P4_2/mnm$, according to CIF no. 1526637 from the COD database.

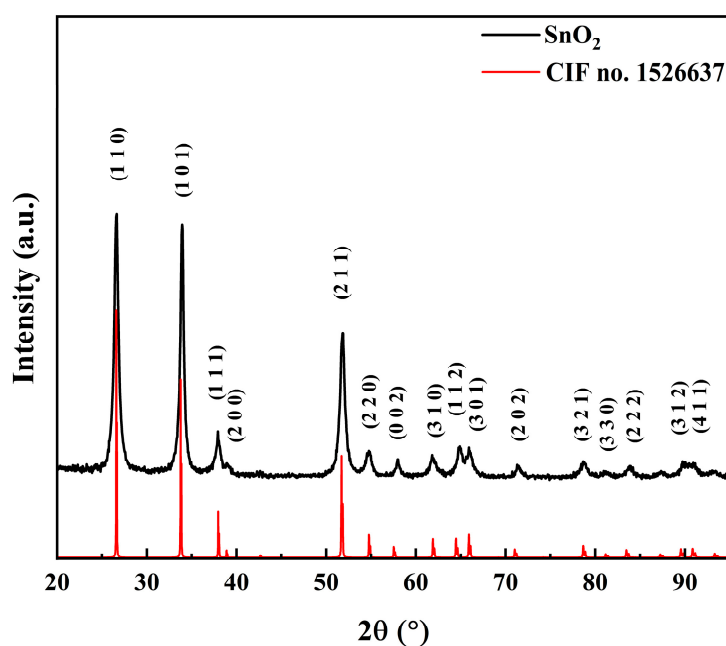


Figure 2. XRD pattern of SnO_2 .

Through Rietveld refinement, using the MAUD version 2.99 software, the lattice parameters and the average crystallite size of $21.47 \pm 0.19\text{ nm}$ were determined. The crystallographic parameters for the lattice are slightly different than the reference data.

3.2. Analytical TEM Characterisation

The low-magnification TEM images were used to characterise the sample's morphology. Figure 3a shows that the sample consists of nanoparticles with the following different dimensions: smaller quasi-spherical nanoparticles (having $\sim 9\text{ nm}$) and larger elongated nanoparticles (having $\sim 35\text{ nm}$).

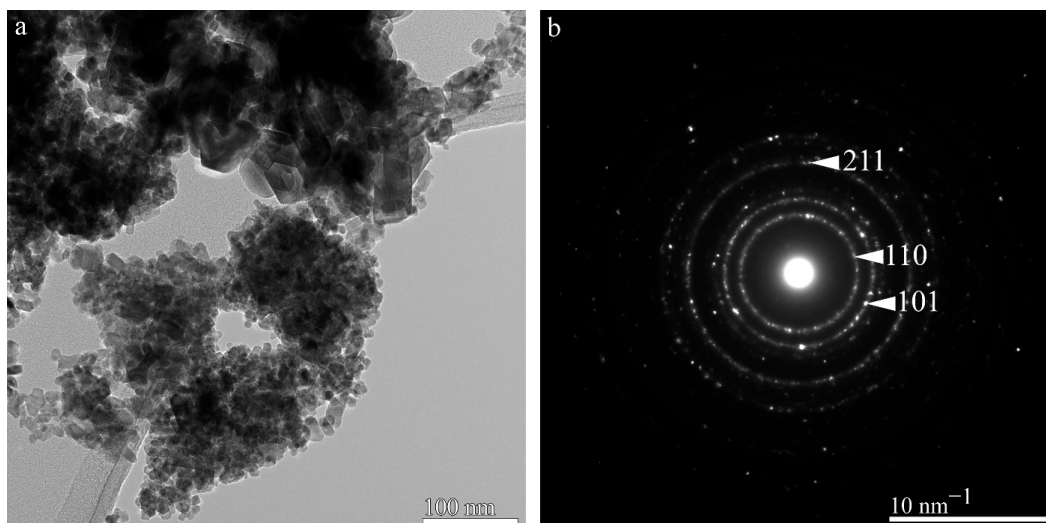


Figure 3. TEM image of SnO₂ (a) and the corresponding SAED pattern, revealing the tetragonal structure of SnO₂ (b).

The structure of the sample was determined using selected area electron diffraction (SAED). The SAED pattern shown in Figure 3b is typical for a polycrystalline material, and it reveals the tetragonal structure of SnO₂, with the space group P4₂/mnm. The white arrows are pointing towards crystallographic planes (110), (101), and (211), as indexed according to cif no. 2104754 from COD database.

The high-resolution TEM (HRTEM) investigations revealed the presence of (110) and (101) crystallographic facets (Figure 4). Kuncser et al. [20], using VESTA modelling, showed that (110) and (101) facets mostly have oxygen terminations.

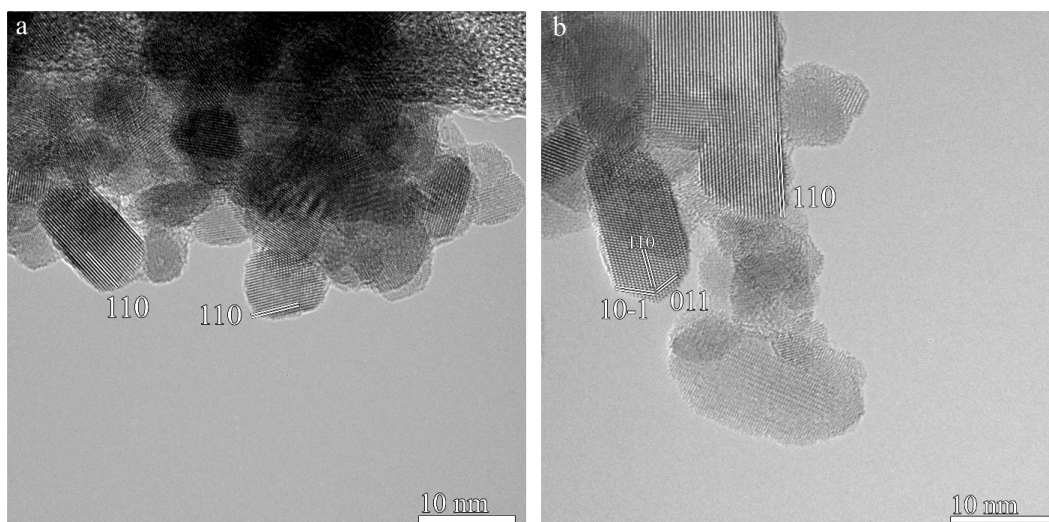


Figure 4. HRTEM images showing faceted nanoparticles having different dimensions.

Figure 4a shows two nanoparticles having the edges along (110) crystallographic planes. The double white lines in Figure 4b indicate the (110), (10-1), and (011) crystallographic planes of a nanoparticle oriented along the [1-11] axis.

The average dimension was determined by measuring ~400 nanoparticles using low-magnification TEM images similar to the TEM image shown in Figure 3a. The size distribution is shown in Figure 5. After fitting the as-obtained histogram with a log-normal function, we obtained a mean value of 15.4 nm and a standard deviation of 6.9 nm. Within the error limits, the mean value of the particle size obtained from TEM is in accordance with the value of the crystallite size obtained from Rietveld refinement.

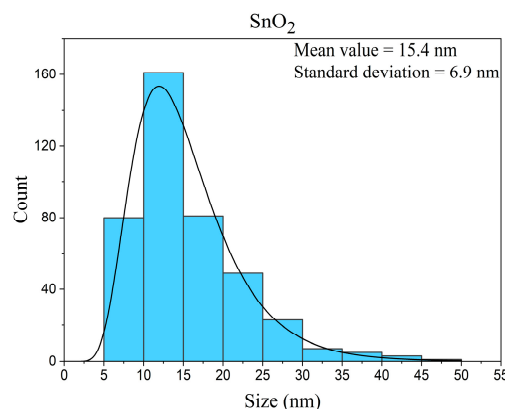


Figure 5. SnO₂ nanoparticles size distribution histogram fitted using a log-normal function.

In conclusion, the morpho-structural TEM investigations have shown that the sample consists of nanoparticles with different dimensions, having well-defined facets along (110) and (101) crystallographic planes [21–23].

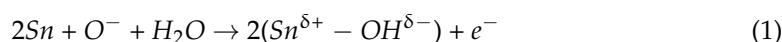
3.3. Sensing Characterisation

The response of MOS sensors depends on the operating temperature of the gas-sensitive material, which determines the adsorption of atmospheric oxygen in its molecular or ionic forms. The response capacity decreases at higher working temperatures due to the different rates of the adsorption/desorption processes [24]. Consequently, we conducted an initial experiment to observe the changes in the sensor signal as the operating temperature varied in the range of 100–400 °C for sensors based on SnO₂ thick layers deposited onto interdigital Pt electrodes with alternative gaps of 100 and 30 µm. The sensor signal was determined by calculating the ratio of the electrical resistance measured under a reference atmosphere (e.g., a synthetic air 5.0 background with 50% relative humidity) to the electrical resistance measured while exposed to 3000 ppm of CO₂ under the same RH conditions. The highest level of sensitivity was achieved at an operating temperature of 350 °C (Figure 6a).

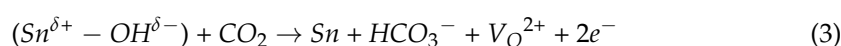
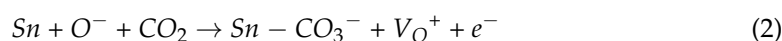
When the sensors operate at moderate temperatures, oxygen physisorption on the MOS surface is generally accepted. This process does not entail any transfer of electrical charge from the sensitive material to the adsorbed molecular oxygen. When the temperature rises, oxygen chemisorption occurs at the surface of the SnO₂ grains. Consequently, electron-depleted layers are formed near the surface of the grains due to the electron transfer from the sensitive material to the adsorbed O[−] oxygen species. In terms of energy, the depleted layers act as potential barriers, impeding the flow of electrons between the boundaries of the grains [25].

Considering the interdigital gap as $d \approx N \times g$ (where N is the number of grains and g is the average grain size), the larger d is, the more grains we have and thus the more intergranular barriers. From the electrical point of view, this situation is associated with electrical resistance in dry air conditions, explaining the higher resistance in the case of SnO₂ deposited on the substrate with an interdigital gap of 100 µm (Figure 6b).

In humid conditions, the electrical resistance decreases due to the known reducing effect of RH [26].



A similar behaviour is related to the presence of CO₂, although it is known as a rather inert gas [27]. Herein, the resistance of SnO₂ decreases under CO₂ exposure, suggesting interactions with previously chemisorbed O[−] (Equation (2)) or OH[−] (Equation (3)) species, leading to the release of electrons in CB.



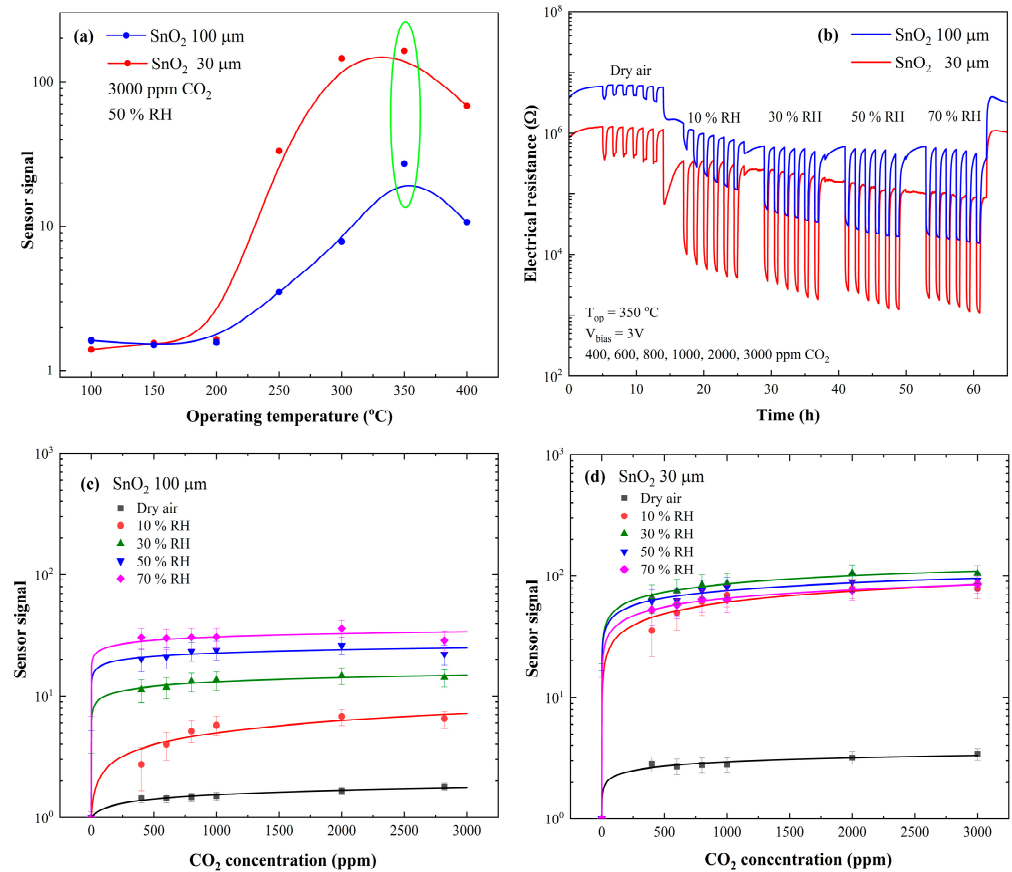


Figure 6. The dependence of the sensor signal on the operating temperature (a), the behaviour of the electrical resistance in the atmosphere with variable RH and CO₂ concentrations for an operating temperature of 350 °C (b), and the sensor signal to CO₂ for SnO₂ 100 μm versus SnO₂ 30 μm (c,d).

Translating the electrical resistance changes in the sensor signals for both sensitive structures (Figure 6c,d), it can be observed that the smaller interdigital gap (30 μm), the higher the sensor signal is. Moreover, one can see that both sensors exhibit a special relation with water, as long as the CO₂ sensitivity increases in the presence of RH compared to dry air. Complex phenomenological investigations (e.g., simultaneous electrical resistance and contact potential differences) provide the perspective of an explanation regarding this behaviour (Figure 7).

The CPD measurements provide insights into the changes in work function ($\Delta\Phi$), allowing us to discriminate between physisorption (associated with changes in the electronic affinity, $\Delta\chi$) and ionosorption (associated with changes in the surface potential barrier, $q\Delta V_s$). Considering the electrochemical potential (μ) of the SnO₂ constant, we can write

$$q \times \Delta CPD = \Delta\Phi = \Delta\chi + q\Delta V_s = \Delta\chi - k_B T \ln R_{air}/R_{gas} \tag{4}$$

where q is the electron charge, ΔCPD is the contact potential difference measured with the Kelvin Probe, k_B is the Boltzmann constant, T is the operating temperature, R_{air} is the electrical resistance measured under humid synthetic air, and R_{gas} is the electrical resistance measured under CO₂ exposure.

As shown in Figure 7a,b, $\Delta\Phi$ does not vary because it is the same SnO₂ material deposited onto substrates with different interdigital gaps. On the other hand, the greater the water effect ($\Delta\chi$), the greater the potential barrier variation ($q\Delta V_s$).

At this point, it is important to understand whether the differences induced by the interdigital gap are determined by their electrical contribution to the total resistance of the sensors or by the catalytic activity of the platinum electrodes.

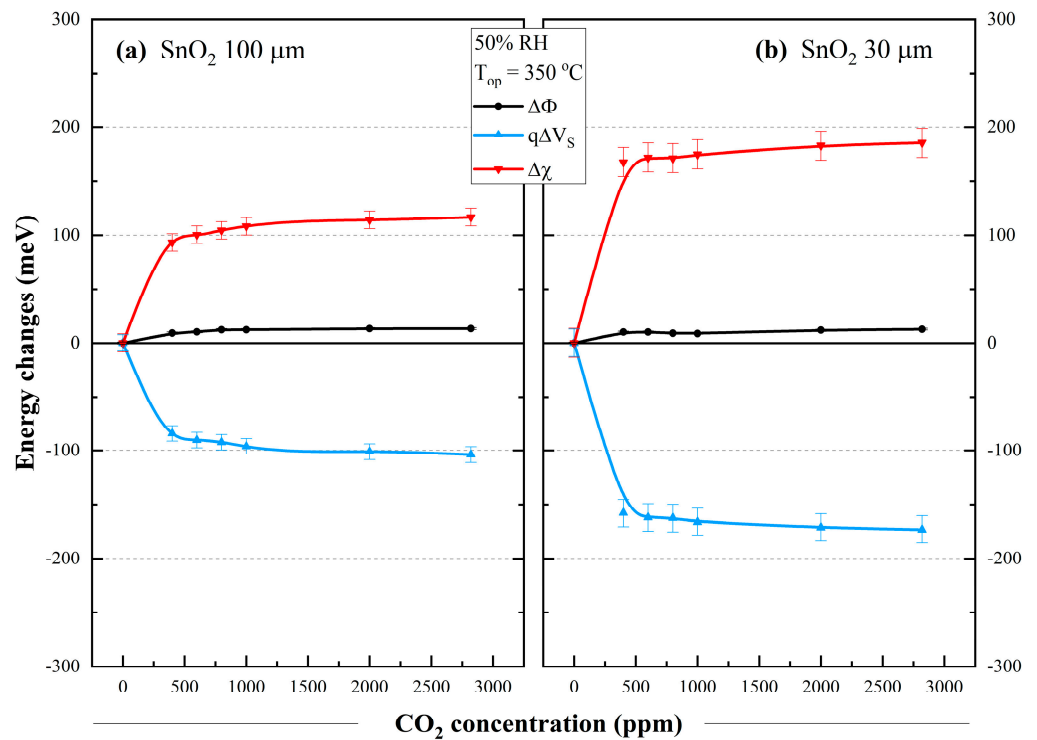


Figure 7. CO₂ influence over the potential changes: SnO₂ 100 μm (a) and SnO₂ 30 μm (b) for T_{op} = 350 °C and 50% RH.

The first hypothesis is supported by the geometrical approach of a SnO₂ polycrystalline sensitive material, considering incompletely depleted grains, arranged between Pt electrodes with interdigital gaps (*L*) of 100 and 30 μm (Figure 8a). The so-called surface state model [28] was used to represent the surface and bulk energetic dependencies with respect to the percolation path phase of the electric current (Figure 8b).

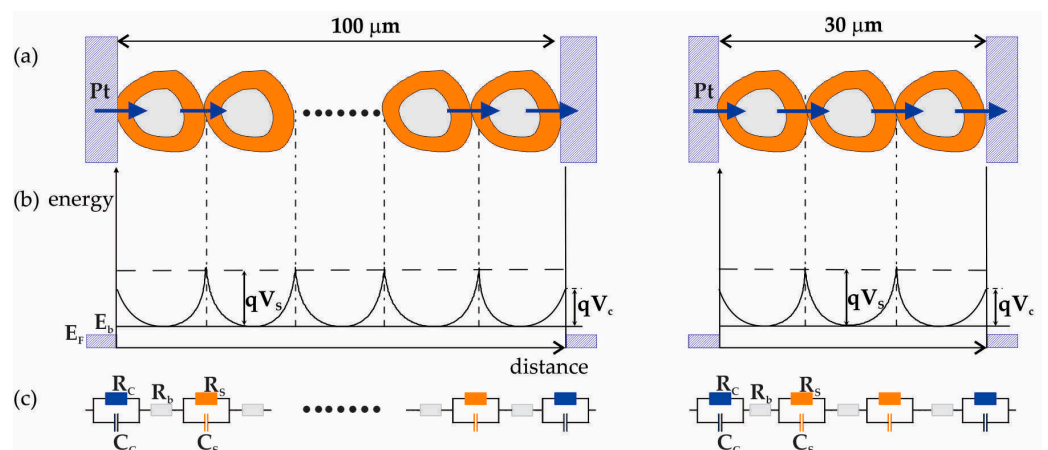


Figure 8. Schematic representation of the sensitive structure based on SnO₂ deposited on a substrate with Pt electrodes with different interdigital gaps *L* (a), energy band bending (b), and the equivalent electrical circuit (c).

For gas sensors consisting of a thick polycrystalline-sensitive MOS layer, the conduction mechanism is dominated by surface phenomena. Exposure to an in-field-like atmosphere and operating temperature favours oxygen and water vapour chemisorption, determining the covering of the surface with the negative charge. This causes the appearance of a depletion layer near the surface due to the Coulomb repulsion towards the electrons in the bulk. Thus, the conduction is limited by the Schottky barriers (qV_s) formed

at the grain boundaries. In terms of the electrical equivalent circuit (EEC), the surface is associated with a resistance R_s in parallel with a capacity C_s (Figure 8c). These are controlled by the charging/discharging of the surface traps which are directly modulated by the surface chemical gas interactions [29].

The resistance R_b corresponds to the electrons in the bulk and is weakly influenced [30]. The SnO_2 -Pt electrode contact is associated with the $R_c C_c$ parallel circuit.

The electrons will flow from the semiconductor towards the metal because the SnO_2 work function (4.53 eV) is lower than the Pt work function (5.64 eV) [31,32]. Accordingly, the energy bands bend up due to the depletion of electrons in the semiconductor, and the electrons flowing towards the Pt electrode must cross over the potential barrier qV_c , as in the case of the grain-to-grain Schottky element. But, taking into account that the Pt resistance is much lower than the SnO_2 surface resistance ($R_c \ll R_s$), its contribution can be neglected, whether the interdigital gap L is 100 or 30 μm .

By close observation and through the aforementioned reasons, the electrical influence of the interdigital electrodes on a thick film gas sensor can be considered negligible.

The second hypothesis is supported by the known spill-over effect of Pt [33,34]. In brief, when a reducing gas is adsorbed on Pt, its dissociation is activated, followed by migration (spill-over) on the MOS surface where it interacts with oxygen, increasing the conductivity in the case of an n-type semiconductor [35].

In addition to the effects induced by impregnation/doping with noble metals, the role of Pt electrodes must be considered in terms of the geometric and catalytic effects. Several authors [36,37] have pointed out the significant role of the geometry influence of the electrodes placed at the bottom region of the sensitive MOS layer. When a certain gas molecule hits the MOS surface, it diffuses through the porous film and induces an electrical effect at the bottom electrodes (so-called "three-phase boundary regions"). Starting from the empiric demonstration of the differences in sensitivity induced by the variation in the electrode gaps, Hofer et al. [38,39] propose a rigorous work aiming to establish precisely the role of interdigital geometry on the sensing performance. As such, a sensor array with a highly asymmetric electrode configuration could develop a low-cost sensor system with improved selectivity (e.g., the selective detection of NO_2 versus CO by varying the interdigital electrode gaps).

On the other hand, the Pt electrode shows increased activity in the direct conversion of CO_2 , with implications on the electrical properties of the SnO_2 sensitive layer [40]. Besides direct conversion, the spillover effect activates the gas adsorption on the Pt, which subsequently leads to the diffusion or migration of the adsorbed species on the neighbouring grains [41]. By spanning the literature, one can find that the chemical activation of CO_2 as a quite inert gas is still a matter of debate, especially with MOS-based gas sensors. The complex work of Wang et al. [42] stated that Pd and Pt represent the most favourable metals for CO_2 conversion. The role of Pt as a single-atom catalyst has attracted extensive attention due to the superior catalytic performance towards CO_2 conversion via a reverse water gas shift reaction (RWGS). Thus, the work of He et al. [43] presented a simple route to load 6.4 wt %Pt on silicon carbide with superior catalytic properties. Mondoza-Núñez et al. [44] investigated the effect of Pt addition on CO_2 methanation catalysed by ZrO_2 -supported Rh. Quite similar results have been obtained by Ramos Gonzalez et al. [40] on pristine Pt-catalysed SnO_2 hybrid nanostructures when operated at low temperatures (100 °C), envisaging a gas sensing mechanism based on the adsorption of OH^- ions onto the SnO_2 surface. The sensing mechanism was attributed to the electron transfer from the porous silicon-based band to the conduction band of the SnO_2 . In the case of ZnO nano-ribbons [45], the role of Pt was used alongside Pd, Fe, Ag, and Au as simple adatom catalysts towards sensing H_2 , H_2S , and CO_2 .

With the aforementioned review of the literature and considering the technological details of our samples (Figure 9), it is beyond doubt that the noble parts of the sensor (e.g., at the three-phase boundary between gas–Pt interdigital electrodes and SnO_2) have a great share in the catalytic activity of the CO_2 gas.

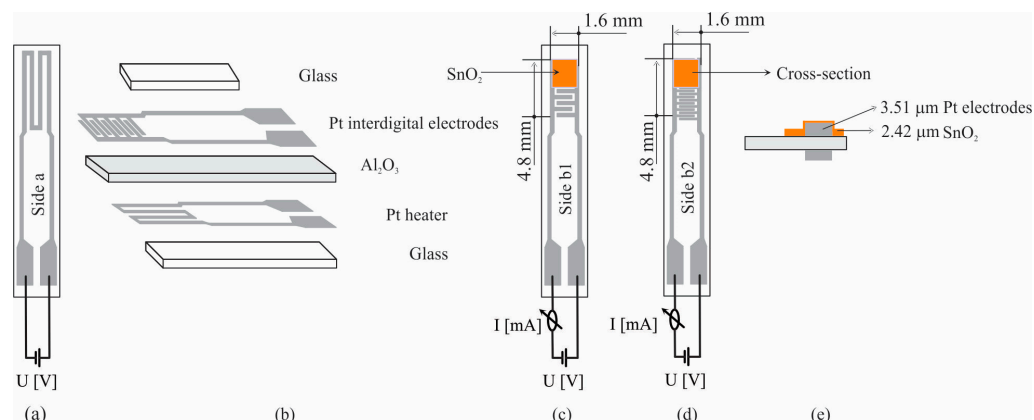


Figure 9. Planar substrate sensor overview. Side a represents the Pt heater meander (a) and sensor components parts (b); Side b1 represents the interdigital electrodes with a 100 μm gap (c); Side b2 represents the interdigital electrodes with a 30 μm gap (d) and a cross-section of the sensor (e).

Specifically, the thickness of the SnO_2 layer (2.42 μm) and the Pt electrodes (3.51 μm) was determined with the Ambios XP-100 Profilometer, and their ratio suggests that the dominating amount of Pt controls the overall sensing effect.

It is worth mentioning that besides the Pt interdigital electrodes (e.g., where solely catalytic effects take place), other Pt regions are covered with glass to avoid parasitic CO_2 catalytic effects.

In this context, we strongly believe that the sensitivity to CO_2 increases with the proportion of Pt in the sensitive structure. This explains the higher sensor signal when SnO_2 is deposited over electrodes with an interdigital distance of 30 μm , compared to 100 μm .

These results are consistent with the results from the literature which highlights the role of Pt in CO_2 reactivity; although, in the field of chemical sensors, the findings are less true for MOS-sensitive materials.

4. Conclusions

SnO_2 powder was obtained by hydrothermal growth at a temperature of 160 $^\circ\text{C}$. A final thermal treatment at 550 $^\circ\text{C}$ has completed the synthesis processes. X-ray diffraction has shown a tetragonal structure, and the Rietveld refinement revealed a crystallite size of $\sim 21.5 \pm 0.19$ nm. The morpho-structural TEM/HRTEM investigations highlight nanoparticles with different dimensions, having a mean value of 15.4 nm for a standard deviation of 6.9 nm and well-defined facets along (110) and (101) crystallographic planes. The SnO_2 powder was transformed into a paste by mixing it with 1,2 Propanediol, and then it was screen-printed as a thick layer onto commercial Al_2O_3 substrates having Pt electrodes with alternative interdigital gaps of 100 μm and 30 μm . The obtained sensors labelled “ SnO_2 100 μm ” and “ SnO_2 30 μm ” were thermally treated at 500 $^\circ\text{C}$ in air to eliminate the organic solvent and ensure SnO_2 adhesion to the substrate. The electrical power through the substrate backside heater controlled the temperature of the SnO_2 layer, favouring the chemical interaction with gases. A Gas Mixing System was used to simulate the in-field-like test atmosphere (synthetic air having different relative humidity and CO_2 concentration). The contact potential differences (CPDs) induced by the chemical interactions on the SnO_2 surface were recorded using a McAllister 6500 Kelvin Probe. Thus, it was possible to differentiate between water physisorption associated with changes in the electronic affinity and oxygen ionosorption associated with changes in the surface potential barrier and, consequently, with the electrical resistance. The differences induced by the interdigital gap over the sensor signal to CO_2 were analysed in terms of the electrical equivalent circuit and catalytic activity of the platinum electrodes. The thickness ratio of 2.42 μm /3.51 μm between the SnO_2 layer and the Pt electrodes allowed us to conclude that the amount of Pt

specific for a 30 μm interdigital gap determines the increase in the sensing response to CO_2 in accordance with the catalytic effect reported in the literature.

Author Contributions: Methodology, writing—review and editing, funding acquisition, A.S.; investigation, writing—original draft, A.C.I.; investigation, writing—original draft, C.G.M.; formal analysis, writing—review and editing, I.V.D.; investigation, validation, O.G.F.; methodology, writing—original draft, I.D.V.; conceptualization, writing—original draft, writing—review and editing, C.E.S. All authors have read and agreed to the published version of the manuscript.

Funding: This research was funded by the Ministry of Research, Innovation and Digitization CNCS-UEFISCDI through the project PN-III-P4-PCE-2021-0384 within PNCDI III and the Core Program within the National Research Development and Innovation Plan 2022–2027, carried out with the support of the Ministry of Research, Innovation and Digitization, project no. PC1-PN23080101. The contribution of Catalina G. Mihalcea (C.G.M.) to this work is part of the PhD “Nanostructured materials for gas sensing: correlations between functional, electronic and microstructural properties” supported by CERIC-ERIC.

Institutional Review Board Statement: Not applicable.

Informed Consent Statement: Not applicable.

Data Availability Statement: Data are available on request from the authors.

Conflicts of Interest: The authors declare no conflicts of interest. The funders had no role in the design of the study; in the collection, analyses, or interpretation of data; in the writing of the manuscript, or in the decision to publish the results.

References

1. Taguchi, N. Gas Detecting Device. U.S. Patent US3695848A, 3 October 1972.
2. Kong, Y.; Li, Y.; Cui, X.; Su, L.; Ma, D.; Lai, T.; Yao, L.; Xiao, X.; Wang, Y. SnO_2 nanostructured materials used as gas sensors for the detection of hazardous and flammable gases: A review. *Nano Mater. Sci.* **2022**, *4*, 339–350. [[CrossRef](#)]
3. Zheng, Z.; Wang, Y.-S.; Wang, M.; Zhao, G.-H.; Hao, G.-P.; Lu, A.-H. Anomalous enhancement of humid CO_2 capture by local surface bound water in polar carbon nanopores. *Nat. Commun.* **2024**, *15*, 8919. [[CrossRef](#)]
4. Ramanathan, S.; Malarvili, M.B.; Gopinath, S.C.B. Assessing respiratory complications by carbon dioxide sensing platforms: Advancements in infrared radiation technology and IoT integration. *Arab. J. Chem.* **2023**, *16*, 104478. [[CrossRef](#)]
5. Fleming, L.; Gibson, D.; Song, S.; Li, C.; Reid, S. Reducing N_2O induced cross-talk in a NDIR CO_2 gas sensor for breath analysis using multilayer thin film optical interference coatings. *Surf. Coat. Technol.* **2018**, *336*, 9–16. [[CrossRef](#)]
6. Zubair, M.; Chen, S.; Ma, Y.; Hu, X. A Systematic Review on Carbon Dioxide (CO_2) Emission Measurement Methods under PRISMA Guidelines: Transportation Sustainability and Development Programs. *Sustainability* **2023**, *15*, 4817. [[CrossRef](#)]
7. Almawgani, A.H.M.; Fathy, H.M.; Elsayed, H.A.; Ali, Y.A.A.; Mehaney, A. A promising ultra-sensitive CO_2 sensor at varying concentrations and temperatures based on Fano resonance phenomenon in different 1D photonic crystal designs. *Sci. Rep.* **2023**, *13*, 15028. [[CrossRef](#)]
8. Maier, C.; Egger, L.; Köck, A.; Reichmann, K. A Review of Gas Sensors for CO_2 Based on Copper Oxides Their Derivatives. *Sensors* **2024**, *24*, 5469. [[CrossRef](#)]
9. Molino, D.; Ferraro, G.; Lettieri, S.; Zaccagnini, P.; Etzi, M.; Astorino, C.; Nardo, E.D.; Bartoli, M.; Lamberti, A.; Pirri, C.F.; et al. Enhanced CO_2 Detection Using Potentiometric Sensors Based on PIM-1/DBU Imidazolate Membranes. *Adv. Sustain. Syst.* **2024**, 2400415. [[CrossRef](#)]
10. Steinger, F.; Revsbech, N.P.; Koren, K. Total Dissolved Inorganic Carbon Sensor Based on Amperometric CO_2 Microsensor and Local Acidification. *ACS Sens.* **2021**, *6*, 2529–2533. [[CrossRef](#)]
11. Héraly, F.; Sikdar, A.; Chang, J.; Yuan, J. Capacitive CO_2 sensor made of aminated cellulose nanofibrils: Development and optimization. *New J. Chem.* **2024**, *48*, 6064–6070. [[CrossRef](#)]
12. Wang, C.; Ding, Y.; Li, M.; Li, H.; Xu, S.; Li, C.; Qian, L.; Yang, B. Surface acoustic wave sensor based on Au/ TiO_2 /PEDOT with dual response to carbon dioxide and humidity. *Anal. Chim. Acta* **2022**, *1190*, 339264. [[CrossRef](#)]
13. Park, K.; Koh, M.; Yoon, C.; Kim, H.; Kim, H. The behavior of quartz crystal microbalance in high pressure CO_2 . *J. Supercrit. Fluids* **2004**, *29*, 203–212. [[CrossRef](#)]
14. Domènech-Gil, G.; Samà, J.; Fàberga, C.; Gràcia, I.; Cané, C.; Barth, S.; Romano-Rodríguez, A. Highly sensitive SnO_2 nanowire network gas sensors. *Sens. Actuators B Chem.* **2023**, *383*, 133545. [[CrossRef](#)]
15. Casanova-Chafer, J.; Garcia-Aboal, R.; Llobet, E.; Atienzar, P. Enhanced CO_2 sensing by oxygen plasma treated perovskite-graphene nanocomposites. *ACS Sens.* **2024**, *9*, 830–839. [[CrossRef](#)] [[PubMed](#)]
16. Jiao, A.; Zhang, Y.; Yang, L.; Zhao, X.; Wu, C.; Chen, T.; Zhan, R.; Huang, Z.; Lin, H. Enhanced CO_2 response of $\text{La}_{1-x}\text{FeO}_{3-\delta}$ perovskites with A-site deficiency synthesized by flame spray pyrolysis. *Ceram. Int.* **2023**, *49*, 591–599. [[CrossRef](#)]

17. Chavali, M.S.; Nikolova, M.P. Metal oxide nanoparticles and their application in nanotechnology. *SN Appl. Sci.* **2019**, *1*, 607. [[CrossRef](#)]
18. Batzill, M. Surface Science Studies of Gas Sensing Materials: SnO₂. *Sensors* **2006**, *6*, 1345–1366. [[CrossRef](#)]
19. Xiong, Y.; Xue, Q.; Ling, C.; Lu, W.; Ding, D.; Zhu, L.; Li, X. Effective CO₂ detection based on LaOCl-doped SnO₂ nanofibers: Insight into the role of oxygen in carrier gas. *Sens. Actuators B Chem.* **2017**, *241*, 725–734. [[CrossRef](#)]
20. Kuncser, A.C.; Vlaicu, I.D.; Dinu, I.V.; Simion, C.E.; Iacoban, A.C.; Florea, O.G.; Stanoiu, A. The impact of the synthesis temperature on SnO₂ morphology and sensitivity to CO₂ under in-field conditions. *Mater. Lett.* **2022**, *325*, 132855. [[CrossRef](#)]
21. Sopiha, K.V.; Malyi, O.I.; Persson, C.; Wu, P. Chemistry of Oxygen Ionosorption on SnO₂ Surfaces. *ACS Appl. Mater. Interfaces* **2021**, *13*, 33664–33676. [[CrossRef](#)]
22. Masuda, Y. Recent advances in SnO₂ nanostructure based gas sensors. *Sens. Actuators B Chem.* **2022**, *364*, 131876. [[CrossRef](#)]
23. Masuda, Y. Facet controlled growth mechanism of SnO₂ (101) nanosheet assembled film via cold crystallization. *Sci. Rep.* **2021**, *11*, 11304. [[CrossRef](#)] [[PubMed](#)]
24. Rescalli, A.; Marzorati, D.; Gelosa, S.; Cellesi, F.; Cerveri, P. Temperature Modulation of MOS Sensors for Enhanced Detection of Volatile Organic Compounds. *Chemosensors* **2023**, *11*, 501. [[CrossRef](#)]
25. Barsan, N.; Weimar, U. Conduction Model of Metal Oxide Gas Sensors. *J. Electroceram.* **2001**, *7*, 143–167. [[CrossRef](#)]
26. Barsan, N.; Koziej, D.; Weimar, U. Metal oxide-based gas sensor research: How to? *Sens. Actuators B Chem.* **2007**, *121*, 18–35. [[CrossRef](#)]
27. Staerz, A.; Weimar, U.; Barsan, N. Current state of knowledge on the metal oxide based gas sensing mechanism. *Sens. Actuators B Chem.* **2022**, *358*, 131531. [[CrossRef](#)]
28. Morrison, S.R. *The Chemical Physics of Surfaces*; Springer: New York, NY, USA, 1990. [[CrossRef](#)]
29. Franke, M.E.; Koplín, T.J.; Simon, U. Metal and Metal Oxide Nanoparticles in Chemiresistors: Does the Nanoscale Matter? *Small* **2006**, *2*, 36–50. [[CrossRef](#)]
30. Oprea, A.; Bârsan, N.; Weimar, U. Work function changes in gas sensitive materials: Fundamentals and applications. *Sens. Actuators B Chem.* **2009**, *142*, 470–493. [[CrossRef](#)]
31. Islam, M.N.; Hakim, M.O. Electron affinity and work function of polycrystalline SnO₂ thin film. *J. Mater. Sci. Lett.* **1986**, *5*, 63–65. [[CrossRef](#)]
32. Hölzl, J.; Schulte, F.K. Work Functions of Metals. In *Solid Surface Physics*; Hölzl, J., Schulte, F.K., Wagner, H., Eds.; Springer: Berlin/Heidelberg, Germany, 1979. [[CrossRef](#)]
33. Nulmi, S.; Thangadurai, V. Editors' Choice—Review—Solid-State Electrochemical Carbon Dioxide Sensors: Fundamentals, Materials and Applications. *J. Electrochem. Soc.* **2020**, *167*, 037567. [[CrossRef](#)]
34. Yuan, G.; Zhong, Y.; Chen, Y.; Zhuo, Q.; Sun, X. Highly sensitive and fast-response ethanol sensing of porous CO₃O₄ hollow polyhedral via palladium reined spillover effect. *RSC Adv.* **2022**, *12*, 6725–6731. [[CrossRef](#)] [[PubMed](#)]
35. Goel, N.; Kunal, K.; Kushwaha, A.; Kumar, M. Metal oxide semiconductors for gas sensing. *Eng. Rep.* **2023**, *5*, e12604. [[CrossRef](#)]
36. Simion, C.E.; Mihalcea, C.G.; Iacoban, A.C.; Dinu, I.V.; Predoi, D.; Vlaicu, I.D.; Florea, O.G.; Stanoiu, A. Influence of Synthesis Method and Electrode Geometry on GHG-Sensing Properties of 5%Gd-Doped SnO₂. *Chemosensors* **2024**, *12*, 148. [[CrossRef](#)]
37. Lee, S.P. Electrodes for Semiconductor Gas Sensors. *Sensors* **2017**, *17*, 683. [[CrossRef](#)]
38. Hofer, U.; Steiner, K.; Wagner, E. Contact and sheet resistance of SnO₂ thin films from transmission-line model measurements. *Sens. Actuators B Chem.* **1995**, *26*, 59–63. [[CrossRef](#)]
39. Hofer, U.; Böttner, H.; Wagner, E.; Kohl, C.D. Highly sensitive NO₂ sensor device featuring a JFET-like transducer mechanism. *Sens. Actuators B Chem.* **1998**, *47*, 213–217. [[CrossRef](#)]
40. Gonzalez, D.M.R.; Kumar, Y.; Ramón, J.A.R.; Bogyreddy, N.K.R.; Olive-Méndez, S.F.; Karthik, T.V.K.; Becerra, D.; Pérez-Tijerina, E.; Agarwal, V. CO₂ sensing performance enhanced by Pt-catalyzed SnO₂/porous-silicon hybrid structures. *Sens. Int.* **2022**, *3*, 100165. [[CrossRef](#)]
41. Chai, H.; Zheng, Z.; Liu, K.; Xu, J.; Wu, K.; Luo, Y.; Liao, H.; Debliquy, M.; Zhang, C. Stability of Metal Oxide Semiconductor Gas Sensors: A review. *IEEE Sens. J.* **2022**, *22*, 5470–5481. [[CrossRef](#)]
42. Wang, Y.; Chen, E.; Tang, J. Insight on Reaction Pathways of Photocatalytic CO₂ Conversion. *ACS Catal.* **2022**, *12*, 7300–7316. [[CrossRef](#)]
43. He, Y.; Huang, D. Single-Atom Platinum Catalyst for Efficient CO₂ Conversion via Reverse Water Gas Shift Reaction. *Molecules* **2023**, *28*, 6630. [[CrossRef](#)]
44. Mondoza-Núñez, E.M.; Fierro-Conzalez, J.C.; Zepeda, T.A.; Solis-Garcia, A. Effect of platinum addition on the reaction mechanism of the CO₂ methanation catalyzed by ZrO₂-supported Rh. *Mol. Catal.* **2022**, *533*, 112801. [[CrossRef](#)]
45. Shaheen, A.; Othman, W.; Ali, M.; Tit, N. Catalyst-induced gas-sensing selectivity in ZnO nanoribbons: Ab-initio investigation at room temperature. *Appl. Surf. Sci.* **2020**, *505*, 144602. [[CrossRef](#)]

Disclaimer/Publisher's Note: The statements, opinions and data contained in all publications are solely those of the individual author(s) and contributor(s) and not of MDPI and/or the editor(s). MDPI and/or the editor(s) disclaim responsibility for any injury to people or property resulting from any ideas, methods, instructions or products referred to in the content.